The Influence of Catalyst Layer Thickness on the Performance and Degradation of PEM Fuel Cell Cathodes with Constant Catalyst Loading

Mahdi Darab[1]

Department of Materials Science and Engineering, Norwegian University of Science and Technology (NTNU), N-7491 Trondheim, Norway

Alejandro Oyarce Barnett[2], Göran Lindbergh

Applied Electrochemistry, School of Chemical Science and Engineering, Kungliga Tekniska Högskolan, SE-10044 Stockholm, Sweden

Magnus Skinlo Thomassen[3]

SINTEF Materials and Chemistry, NO-7465 Trondheim, Norway

Svein Sunde[4,*]

Department of Materials Science and Engineering, Norwegian University of Science and Technology (NTNU), N-7491 Trondheim, Norway

Abstract

Three catalytic layers containing Pt nanoparticles supported on high surface area carbon of different Pt loading but with the same total amount of platinum and therefore of different thickness were employed as cathode catalytic layers (CCLs) in a PEM fuel cell. The layers were subjected to a degradation protocol with an upper potential limit of 1.5 V. Upon exposure to the degradation protocol particle size increased, the electrochemical areas (ECAs) of the catalysts decreased, the catalytic layers became thinner, and the average pore size decreased, indicating both carbon and Pt corrosion. The relative decrease in the ECA was approximately the same for all three layers and was therefore approximately independent of CCL thickness. For all samples the reaction order with respect to oxygen was one half and the samples showed doubling of the slope of the potential vs. log current curve ($dE/d\log i$) at high current densities. This indicates that kinetics control the potential at low currents and kinetics and proton migration (ohmic drops in the catalytic layer) at high. However, the degradation protocol also introduced limitations due to oxygen diffusion in the agglomerates. This led to a quadrupling of the $dE/d\log i$-slope in 13% oxygen in the samples with the highest catalyst area per volume. For the sample with the lowest catalyst area per volume this slope increased by a factor of six in 13% oxygen, indicating that the local current density exceeded that required for the Tafel slope of the oxygen-reduction reaction (ORR) to double.

Keywords:
accelerated degradation test, carbon corrosion, slope doubling, reaction order, impedance

1. Introduction

To overcome the cost issue as a major barrier limiting the large-scale commercialization of proton exchange membrane fuel cells (PEMFCs) is a central focus of PEMFC research [1, 2, 3, 4, 5, 6]. An important part of the PEMFC for which substantial cost reductions would be possible is the catalytic layer, which typically consists of carbon material, ionomer and platinum. In a typical PEMFC catalytic layer a Pt electrocatalyst is supported on a carbon black such as Vulcan XC-72 which

---

*Corresponding author. Tel.: +47 735 94051; fax: +47 73 59 11 05

Email address: svein.sunde@material.ntnu.no (Svein Sunde)

[1]Current address: OneSubsea, NO-5024 Bergen, Norway
[2]Current address: SINTEF Materials and Chemistry, NO-7465 Trondheim, Norway
[3]SINTEF Materials and Chemistry, NO-0373 Oslo, Norway
[4]ISE member

has a low cost and high availability. Given the limited availability and high cost of precious metals such as Pt, optimization of catalyst layer structure is of particular importance for large-scale PEMFC deployment. Evidence exists to show that catalyst layer imperfections such as a spot with restricted metal loading have a substantial effect on both membrane-electrode assembly (MEA) performance and durability [7, 8, 9]. This shows the importance of studies on catalyst layers in the larger context of PEMFC commercialization.

The thickness the catalyst layers have been shown experimentally [10, 11, 12, 13, 14, 15] and theoretically [16, 17, 18, 19, 20, 21, 22, 23] to be decisive in determining the performance of the layers. From the data of Wilson and Gottesfeld [24] a thickness of around 4 μm appears to strike an optimum compromise in terms of catalyst utilization and performance for catalyst-coated membrane (CCM) electrodes. Ticianelli and co-workers [10] showed that performance of porous gas diffusion electrodes prepared by impregnating carbon cloth with Pt/C catalysts improved with increasing wt % of Pt in the Pt/C catalyst for a constant total Pt loading of 0.4 mg cm^{-2} and for catalysts of narrow and reasonably similar size distributions. However, these electrodes were impregnated with Nafion$^{\circledR}$ for which the penetration depth into the carbon-cloth support were the same in all cases. Paganini et al. [13] performed similar studies on electrodes prepared by applying catalyst inks to the diffusion layer electrodes by brushing for a number of catalytic layers differing in thickness but with a constant total mass of Pt per geometric area (0.4 mg cm^{-2}). Also in this case did the performance improve with increasing wt % of Pt in the Pt/C catalyst and thus with decreasing thickness of the catalytic layer.

In addition to affecting the effectiveness and overall performance of the catalytic layers the electrochemical characteristics may also change. da Silva and Ticianelli [12] showed that the slopes of the potential vs. log current density curves (i. e. $dE/d \log i$ where E is the potential and i the current density) are very sensitive to the thickness of the catalytic layers, c. f. also Ref. [16]. Characterization of carbon-cloth supported Pt/C electrodes in aqueous solutions of H_2SO_4 demonstrated an increase of the $dE/d \log i$ slope from approximately 70 mV at low current density up to almost four times this value at high current densities. A comparison with theoretical models led to an interpretation according to which various limiting factors kick in at different potentials, including an inherent change in the Tafel slope of the oxygen-reduction reaction (ORR), diffusion limitations in flooded agglomerates containing the catalyst, and ohmic losses in the CCL. Processes at the PEMFC cathode are thus very complex, and complicated transport and electrochemical reaction phenomena are operative in the porous cathode catalytic layer (CCL) simultaneously.

An issue as important as the performance *per se* is the durability of the CCL. Thermodynamically the carbon support is expected to oxidize to CO_2 and CO at potentials higher than 0.2 V vs. the reversible hydrogen electrode (RHE) [25]. On the other hand, under fuel cell operating conditions and cathode potentials around $0.6 - 0.9$ V vs. RHE, the kinetics of carbon corrosion are still quite slow. In practice, potentials higher than 1.2 V vs. NHE are required to corrode the carbon support at sufficiently high reaction rates to cause a significant degradation to the PEMFC electrode [26].

Recent research [27] indicates that the CCL experiences a significant thinning upon being exposed to degradation protocols. It appears however, that few studies exist that investigate the dependence of the stability of PEM-cathodes on initial CCL thickness. It is well known that the potential is not evenly distributed in porous electrodes [28], and therefore there may be a thickness dependence also for CCL stability since stability is related to the (local) potential in the electrode. Degradation also depends on the chemical environment and thus on transport rates, which may differ in a thick electrode from those of a thin. Thus, due to either low proton mobility in the CCL, in the presence of oxygen transport limitations, or both, the electrochemical reaction will occur unevenly in the catalytic layer. Therefore a decrease in the catalyst layer thickness (by design or as a consequence of corrosion) would not necessarily affect the electrochemical performance proportionally. In consequence the effect of current and potential distributions in thick and thin catalyst layers is important in terms of CCL degradation and for which deeper studies are needed. An understanding of such effects will also form an important basis for efforts towards understanding the role of catalyst layer variations [29].

The scope of this work is thus to investigate role of the catalyst layer thickness with respect to degradation and corrosion and MEA electrochemical performance, but with a constant total loading of the catalyst. The cathode was chosen for the study since the rate-determining chemical reaction and the lion's share of the activation overpotential losses take place in this region. Degradation in cathodes therefore merits attention for durability studies of PEMFCs. In this study a well-controlled synthesis technique was used to control the Pt-particle dispersion in the CCL and also to produce samples with almost the same range of particle size to limit the effect of the latter on performance and

durability of the electrocatalysts [30, 31]. The samples were subsequently subjected to accelerated degradation tests (ADTs) by subjecting the cathode to potential between 0.6 V and 1.5 V. Our tests thus differ from those proposed the U.S. Department of Energy (DOE) [32], for example, by exposing the electrode to a more extensive potential range. The DOE tests aim at simulating the gradual degradation of the entire catalyst in normal PEM fuel cell operation. Here, however, we aimed at simulating the effects of typical potential excursions suffered by the cell during start-up/shut-down conditions, under which conditions the cell may be exposed to potentials as high as 1.5 V [33]. We expect these conditions to promote carbon corrosion. The results below will demonstrate that the performance is independent of thickness for a given Pt loading and for typical thicknesses employed in PEM fuel cells. For degradation processes, on the other hand, we aim to show that thickness does matter in layers with a constant total Pt content.

2. Experimental

2.1. Catalyst synthesis

Materials and solvents were obtained from commercial suppliers and were used without further purification. Carbon black (Vulcan XC72, CABOT Corporation), hexachloroplatinate (IV) (Johnson Mattey, Pt content: 39.76 %, purity $\geq$ 99 %), sodium hydroxide (VMR, purity $\geq$ 99 %), ethylene glycol (Sigma-Aldrich purity $\geq$ 99 %) and analytical grade acetone were used to synthesize the catalyst by the adsorption polyol (AP) method explained in detail elsewhere [34, 35]. Briefly, 1.0 g of H_2PtCl_6 was dissolved in 250 ml of ethylene glycol followed by addition of 100 ml of 0.5 mol dm^{-3} NaOH in ethylene glycol to maintain the pH slightly basic. The mixture was then heated at 145 °C for four hours under nitrogen flow. The carbon support was suspended in ethanol by ultra-sonication for 15 minutes, after which the metal colloidal solution was added to the solution. The pH of the mixture was adjusted to around 2 by addition of 1 mol dm^{-3} HCl followed by sonication for another 10 minutes. The mixture was then stirred at 55 °C for 18 hours during which N_2 was bubbled through the suspension. The solution was cooled down and centrifuged. The catalyst was then washed repeatedly with acetone and finally water, and dried at 70 °C for 500 minutes. The same batch of Pt colloidal solution was used for all the metal loadings, viz. for 10% (PtC10), 20% (PtC20) and 30% (PtC30).

2.2. TEM analysis

Transmission electron microscopy (with a JEOL JEM-2010) was performed on the samples to estimate the particle size and study the metal distribution on the support as well as the morphology. TEM was also used to check for presence of aggregates or isolated platinum nanoparticles in the catalysts.

We estimated particle size from the high resolution TEM images, and assuming spherical particles we employed the following equation for the overall surface area, S_{overall},

$$S_{\text{overall}} = \frac{6 \times 10^3}{\rho \times d} \tag{1}$$

where $\rho = 21.4$ g cm^{-3} is the density of Pt and d is the particle size [36].

2.3. Thermal gravimetric analysis

Thermal Gravimetric Analysis (TGA) was conducted on a NETZCH, STA449C thermogravimetric analyzer using a flow of air in the temperature range 25 through 800 °C to determine the actual Pt loadings on the carbon supports.

2.4. MEA fabrication

Nafion$^{\circledR}$ 112 membranes (DuPont) were pre-treated by boiling in 3 % H_2O_2 as well as in 0.5 mol dm^{-3} H_2SO_4 followed by rinsing in boiling Milli-Q water. The ink was prepared by mixing either 10 wt%, 20 wt% or 30 wt% Pt/Vulcan with 5 wt% Nafion$^{\circledR}$ solution (DuPont). Equal amounts Milli-Q water and isopropanol was subsequently added so that the final ink had a constant Pt/C concentration of about 3 wt%. The ink was ultrasonicated for 1 hour and vigorously stirred overnight. The working electrodes (WE) were prepared by spray-painting the pretreated Nafion$^{\circledR}$ 112 membranes placed on a 90 °C hot plate. Electrode loading was determined by comparing the weight difference between the un-coated and Pt-catalyst coated membranes. The achieved Pt loadings were 0.1 mg cm^{-2}, 0.12 mg cm^{-2}, and 0.11 mg cm^{-2} for the 10 wt%, 20 wt% and 30 wt%, respectively and the Nafion® to carbon ratio (N/C) was 0.8. Catalyzed ELAT (ETEK, Inc.) electrodes, used as combined counter and reference electrode (CE/RE), were employed in the anode with 30 wt% Pt/Vulcan XC-72 and Pt loading of 0.5 mg cm^{-3}. The fabrication of MEAs was accomplished by heat-pressing the ELAT electrodes onto the catalyzed Nafion® 112 membranes at 130 °C under a pressure of 3 bar for 5 min. A gas diffusion layer (GDL Sigracet 10BA) was mounted on the WE.

2.5. SEM analysis

SEM imaging was carried out using a Hitachi S-4800 FE Scanning Electron Microscope operated at 1.5 kV accelerating voltage at 8.3 mm and 8.8 mm working distances. The analysis of cross sections of the MEAs were obtained by the freeze and break technique described elsewhere [37]. Pore size distribution of the catalysts were estimated from SEM images using the open-source image software ImageJ [38].

2.6. In-situ electrochemical evaluation

The fuel cell hardware was purchased from Fuel Cell Technology Inc. The sealing pressure applied to the MEAs was 6 MPa. Additionally, the test bench also controlled the temperature of the cell (T_{cell}), the H_2 and O_2/air humidification temperatures ($T_{hum,a}$ and $T_{hum,c}$) as well as the temperature of the pipe (T_{pipes}) connecting the humidifiers (also Fuel Cell Technology Inc.) with the cell. The cell area was 1 cm^2 for all experiments. Cyclic voltammetry and polarization curves were recorded by using a PAR 273A potentiostat. Electrochemical impedance spectroscopy (EIS) measurements were carried out on an Autolab 302N impedance analyzer.

Cyclic voltammograms and CO stripping were obtained at 80 °C using fully humidified gases, sweep rates of 20 mV s^{-1} with a flow rate of 60 ml min^{-1} of N_2 fed to the WE, and 120 ml min^{-1} of 5% H_2/Ar fed to the CE/RE. Due to lower H_2 partial pressure on CE/RE, the presented cyclic voltammograms were corrected with a 45.5 mV shift calculated by the Nernst equation [22]. (The CO-stripping voltammograms and EIS measurements in N_2 are reported below with respect to RHE which in this work refers to the cathode potential vs. the CE/RE, corrected for the Nernst shift, under conditions for which the anode polarization is negligible. The ADT is also specified with respect to the RHE. All other potentials reported below are cell potentials.)

The electrochemical area (ECA) [39] was estimated based on the charge transferred during the electrooxidation of CO monolayers, assuming one CO molecule bonded per Pt atom (Pt-CO$_{ads}$) [40],

$$ECA_{CO}(\text{ cm}^2\text{ g}^{-1}) = \frac{Q(\text{ mC})}{0.42\text{ mC cm}^{-2} \times W_{Pt}(\text{ g})} \quad (2)$$

where Q_{CO} is the charge transferred during the CO oxidation reaction, 420 μC cm^{-2} is the charge required to oxidize CO monolayer bonded with one Pt atom in a linear adsorption configuration and W_{Pt} is the mass of Pt used in the electrode.

To estimate the conductivity of the CCL ionomer, EIS measurements were carried out with N_2 and 5% H_2/Ar on the WE and the CE/RE with flow rates of 60 ml min^{-1} and 120 ml min^{-1}, respectively. EIS spectra were recorded with an amplitude of 10 mV (top) at 0.35 V vs. RHE and in the frequency range 10 kHz through 0.1 Hz.

The polarization curves were recorded at a sweep rate of 1 mV s^{-1} between open circuit potential (OCP) and 0.3 V vs. CE/RE. To investigate the mass transport properties of the cathodes, diluted O_2 was used as oxidant using the same flow rate (120 ml min^{-1}) ensuring equivalent water content at the particular current density in the cell.

The recorded polarization curves were corrected for iR-drop from the high frequency resistance (HFR) of the fuel cell that was obtained for every 100 mA cm^{-2} increment in current density between a 100 kHz and 1 kHz range and applying an AC signal amplitude that was 5% of the dc (direct current) measured. Moreover, extended EIS spectra between 100 kHz – 100 mHz frequencies were also recorded at 0.01, 0.2, 0.5 and 1 A cm^{-2}.

Measurements with diluted O_2 were carried out keeping the total volumetric flow rate constant. All experiments in diluted oxygen were performed at 0.2 A cm^{-2}, at atmospheric pressure and at 80 °C. The air stoichiometry was 133.1 in 100 % oxygen, 81.2 in 61 % oxygen, 42.6 in 32 % oxygen, and 27.9 in 21 % oxygen During the measurements the amount of water in the incoming gases was held constant. In addition, the high relative humidity and low current density also ensured a low degree of membrane and anode dehydration.

2.7. Accelerated degradation test

The CCLs were subjected to accelerated degradation tests (ADTs) consisting of 100 cycles of cathode potentials between 0.6 V and 1.5 V vs. RHE using a sweep rate of 40 mV s^{-1}. The temperature of the cell was set to 80 °C, using fully humidified H_2 at the anode and fully humidified O_2 at the cathode.

3. Results and discussion

3.1. Ex-situ evaluation of synthesized catalyst

Figure 1(a) shows the percentage of initial weight as a function of temperature for PtC10, PtC20 and PtC30 electrocatalysts upon heating as measured by thermal gravimetry. The steep drop around 400 °C for all samples is a signature of carbon oxidation, and the residue is

the platinum content in the specimens. It is seen in Figure 1(a) that the nominal loading is in agreement with the weight percentage of the residue up to 800 °C.
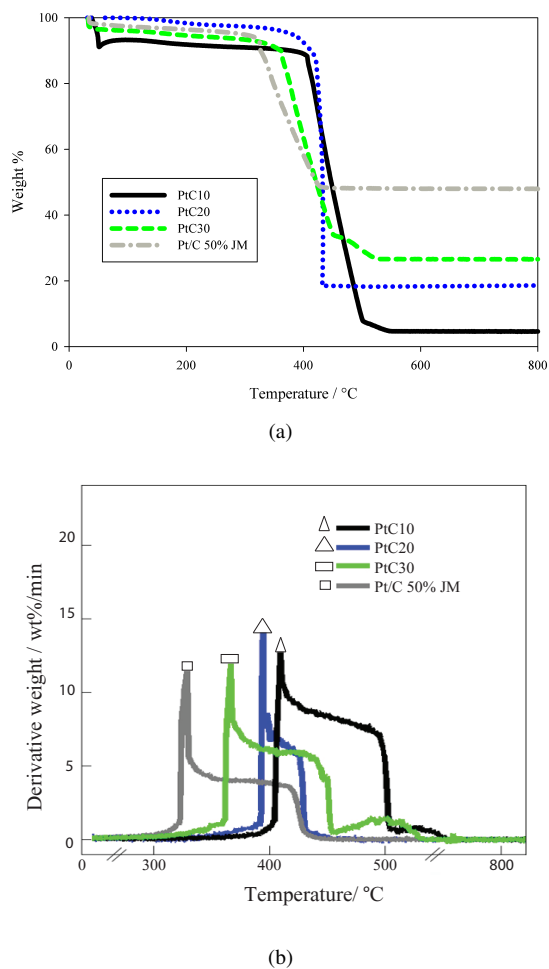

(a)

(b)

Figure 1: (a) Thermal gravimetric analysis (TGA) results for the samples listed in Table 1. The atmosphere was oxygen and the temperature ramp was 10 °C min^{-1}. (b) Temperate programmed oxidation (TPO) results for the samples listed in Table 1. Conditions the same as (1(a)).

The results of temperate programmed oxidation (TPO) for the three catalysts in this study and a commercial benchmark (Pt/C 50% JM) are presented in Figure 1(b). The differences in the peak temperatures in Figure 1(b) for the catalysts indicate different activation energies for carbon reacting to CO_2 and that Pt to a significant degree catalyzes the carbon corrosion reaction. It has been shown that particle size influences TPO peak temperatures, a large particle size leading to high peak temperature and vice versa for a given Pt

loading [41]. The variations in particle size here are of a similar or even larger magnitude as in [41], where the PtC10 sample has the smallest particle diameter and PtC30 the largest. Our results are therefore opposite of those of [41]. However, in our case the loading is not constant, and the results in Figure 1(b) therefore suggest that the differences in peak temperature are due to other factors such as the catalyst loading.
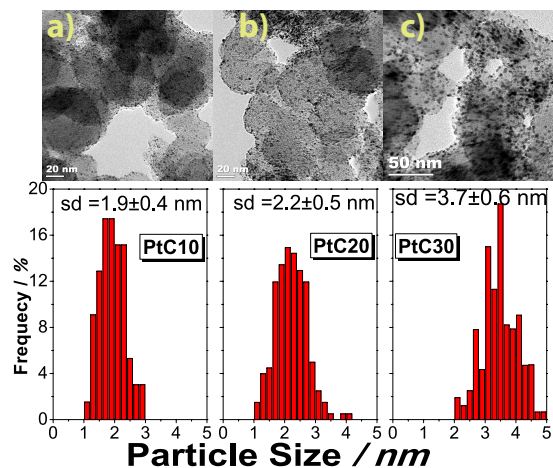

Figure 2: TEM images and corresponding histograms of particle size distribution for the samples a) PtC10, b) PtC20, c) PtC30.

TEM images of the electrocatalysts and the corresponding histograms of particle size distribution are shown in Figure 2. All catalysts appear well dispersed with a particle size around a few nanometers. However, whereas the Pt particles look well separated in PtC10 and PtC20, some minor tendencies towards clustering are apparent in PtC30. The histograms indicate fairly narrow particle distributions. The average particle sizes for the three samples are also summarized in Table 1 and, again, they all seem to be in the same range, that is 1.9 nm, 2.2 nm and 3.7 nm for fresh samples of PtC10, PtC20 and PtC30 respectively. The results demonstrate that although the materials and preparation conditions remain the same, a higher Pt content favors a slightly larger particle size.

Table 1 summarizes the Pt loadings and the estimates of overall surface area and the particle size from the TEM images calculated using Eq. (1).

3.2. Performance in pure O_2

Figure 3 shows the iR-corrected polarization curves for the three MEAs before and after the ADT. The polarization curves are not corrected for the crossover current. PtC20 had a slightly lower cell resistance, as measured from EIS at 1 kHz, than the other two samples.

5

Table 1: Initial properties of the catalysts used in this study including metal loading, platinum particle sizes, and surface areas based Pt-particle size, Eq. (1). All samples were supported on carbon XC-72.

Sample	Pt on C loading	Pt diameter (nm, TEM)	$S_{overall}$ (m^{2}g^{-1})
PtC10	10 wt%	1.9±0.4	147.5±32
PtC20	20 wt%	2.2±0.5	127.4±29
PtC30	30 wt%	3.7±0.6	103.8±24

At 1 A cm^{-2} the values were for example 121, 111, and 124 mΩ cm^2 for the PtC10, PtC20 and PtC30, respectively.

From Figure 3 it appears that all three MEAs have similar initial performance (within ±30 mV at 0.2 A cm^2). The Tafel slopes for the pristine samples are approximately −65 mV for PtC10 and −60 mV for the two others in the low-current range, assuming the reaction is kinetically controlled in this range. At larger currents a change in $dE/d\log i$-slope is apparent, the break between the two regimes being most clearly displayed by Figure 3(a). In the high-current region the slopes are at least twice as large as those in the low-current region. However, these slopes are more accurately evaluated from the Tafel impedance which we will analyse below.

Fuel cell cathodes were modeled mathematically by Perry et al. [42] and Jaouen et al. [43, 44] as oxygen diffusing in flooded agglomerates in which it is reduced by catalysts dispersed there. According to these models, at high currents steady-state polarization curves may display $dE/d\log i$-slopes twice or even four times those at low currents, depending on the factors controlling the current-voltage characteristics. Comparing our curves to those in the modeling papers [42, 43] we assume that the current range with $dE/d\log i$-slope of approximately 65 mV is controlled entirely by kinetics. Figure 3 shows that the $dE/d\log i$-slopes more than double at the higher currents.

A summary of these and other diagnostic criteria are given in Table 2.

As can be seen from Figure 3, the performance of all three CCLs experiences a significant decrease upon the ADT. The effects of performance degradation upon the ADT are more significant at high current densities; At low current densities the performance loss is only a few percent, whereas at high current densities the degradation in performance is quite pronounced for all samples. However, it appears that the degradation of sample PtC10 was somewhat more provoked by the ADT than the other two.

Figure 4 shows the results of EIS measurements at different current densities before and after the ADT. For the sake of clarity, the spectra are plotted as Tafel impedance Z_t (i.e. impedance multiplied with the steady-state current density) [44, Eq. (22)],

$$Z_t = \frac{\tilde{E}}{\tilde{i}} i_{st} \qquad (3)$$

where $\tilde{E}$ is the potential amplitude, $\tilde{i}$ the current-density amplitude (taken here to be positive), and i_{st} the steady state current density. (The ohmic resistance, as assessed from the high-frequency intercept of the impedance-plane plot with the real axis, has been subtracted from all data.) For high current densities the impedance plane plots consist of a single arc, but the spectra at high currents contain two clearly discernible separate arcs along with some inductive features (positive imaginary parts) at low frequencies [45]. Comparing the spectra of the three MEAs before and after the ADT it is clearly observed that the size of all the impedance arcs increase upon the ADT. In this presentation the $dE/d\log i$-slope can be found as the difference between the low-frequency intercept with the real axis and the high-frequency intercept. (A similar use of impedance data was also employed by da Silva and Ticianelli [12].) This assumes that membrane effects are absent (see below), and that a natural logarithm is employed for the Tafel plots, to be multiplied by 2.303 in a base 10-logarithm plot [44]. For all samples the diameter of the arc in the Tafel-impedance plane plot are in good agreement with the slopes from the steady-state curves, Figure 3.

Based on an agglomerate model, Wiezell *et al.* [46] attributed the inductive features to a combination of processes primarily in the anode and the membrane, with only a minor contribution stemming from the cathode [46]. Inductive features associated with the membrane processes are related to water transport and are accompanied by a contribution $idR_m/di < 0$, where R_m is the membrane resistance, to the low-frequency intercept of impedance-plane plots for hydrogen-oxygen PEM fuel cells [47, 48]. However, the membrane resistance in Figure 3 is basically constant with current density, and the magnitude of the inductive effects are small. This suggests that these processes are not significant compared to those at the cathode and the effects

Table 2: Diagnostic criteria for the analysis of polarization curves of gas-diffusion electrodes. A reaction order Ω_{O_2} of one and Tafel slope b_T are assumed for the corresponding polycrystalline electrode. The catalyst surface area per volume is denoted a and the MEA thickness by L_{ct}. Diagnostic criteria collected from Jaouen et al. [43, 44] and Perry [42]. "Kinetics" refers to ORR kinetics at the Pt particles, "diffusion" to diffusion of oxygen in Pt/C agglomerates, and "migration" to ionic migration (ohmic drops in the catalytic layer)

Current range	Slope $dE/d\log i$	Ω_{O_2}	a-dependence	Thickness dependence	Porosity dependence	Governing process(es)
Low	b_T	1	$\propto a$	Proportional	$1 - \epsilon_2$	Kinetics
High	$2b_T$	1	$\propto \sqrt{a}$	Proportional	$1 - \epsilon_2$	Kinetics + diffusion
High	$2b_T$	½	$\propto \sqrt{a}$	Independent	$\sqrt{1 - \epsilon_2}$	Kinetics + migration
High	$4b_T$	½	$\propto a^{1/4}$	Independent	$\sqrt{1 - \epsilon_2}$	Kinetics + diffusion + migration

of the ADT on the latter. Finally, in view of the minor contribution of the anode to the total overpotential we therefore base our interpretation here of the impedance spectra on the low-frequency capacitive arc and in terms of processes in the cathode.

Thus, an increase in the $dE/d\log i$-slope is clearly apparent also from Fig 4. From the impedance data the $dE/d\log i$-slope of sample PtC10 doubles as the current is increased from 10 mA cm^{-2} to 0.2 A cm^{-2} both for the pristine and the sample exposed to the ADT. At 1 A cm^{-2} the $dE/d\log i$-slope is approximately three times that at 10 mA cm^{-2} for the pristine sample. For the PtC10 sample after exposure to the ADT the $dE/d\log i$-slope is quadrupled at 1 A cm^{-2}. A close to quadrupling of the slope was also observed by da Silva and Ticianelli [12], but for electrodes of a total Pt loading per area of approximately four times those employed here.

For the other samples $dE/d\log i$ consistently increased at 1 A cm^{-2} to more than twice that at 10 mA cm^{-2}, but never quadrupled as for sample PtC10.

3.3. Performance as a function of O_2 partial pressure

Figure 5 shows the iR-corrected voltages at 0.2 A cm^{-2} both before and after the ADT as a function of the (base 10) logarithm of the fraction of oxygen in the cathode feed. The voltages of the degraded electrodes are consistently lower than those of the corresponding fresh sample at all oxygen partial pressures. Also, for all samples the voltage increases in direct proportion to the logarithm of the oxygen content, $E \sim \log c_{O_2}$, except for PtC10 at the lowest oxygen fraction for which the curve shows a stronger oxygen dependence. The slopes for the degraded samples are slightly higher than those for the pristine samples.

The oxygen dependence displayed in Figure 5 was analyzed by assuming that the relation

$$ i \propto c_{O_2}^n \exp\{-\eta/b_e\} \tag{4} $$

applies, where η is the overpotential and b_e the slope $dE/d\ln i$, i.e. on a natural logarithm basis. Expanding η as $E - E^{eq}$ where E^{eq} is the electrode equilibrium potential (assuming the anode to act as a pseudoreference electrode) we obtain

$$ n = \frac{1}{b_e}\left[\frac{\partial E}{\partial \ln c_{O_2}} - \frac{\partial E_{eq}}{\partial \ln c_{O_2}}\right] \tag{5} $$

at constant current and where $\partial E_{eq}/\partial \ln c_{O_2} \sim$ 60 mV/2.303 [49, 50]. Through the results in Figure 5 we estimate the slopes $\partial E/\partial \ln c_{O_2}$ to be approximately 65 mV for all samples and pressures, except at low p_{O_2} for the degraded sample PtC10. In this case the slope appears to be approximately twice this value. With $b_e \sim 60$ mV at 0.2 mA cm^{-2} (calculated from difference between the high- and low-frequency intercepts in the impedance diagrams) this gives $n \sim 0.6$. In view of the approximations made this is fairly consistent with a reaction order of one half with respect to oxygen, and consistent with the polarization curves being dominated by Tafel kinetics in the low current range and by Tafel kinetics and proton migration in the current range where the $dE/d\log i$-slope is doubled rather than Tafel kinetics and oxygen diffusion in agglomerates [43]. These conclusions contrast those made by da Silva and Ticianelli [12] who obtained the result that diffusion limitations in the film and in the agglomerates also play a role at high current densities in carbon-cloth based electrodes.

Figure 6 shows the impedance spectra at 100% O$_2$ and 13% O$_2$, both before and after the ADT. All the spectra are dominated by a single depressed semicircle-like loop, for some of the samples extending into positive (inductive) imaginary parts at low frequencies as described above. No clear trend in these inductive features with layer thickness can be discerned, whereas the capacitive part of the loop (negative imaginary parts) appears to be significantly affected. For all fresh MEAs there is an increase in the radius of the capacitive semicircle as O$_2$ concentration decreases. As the sample

7

is degraded, the semicircle radius increases for a given partial pressure of oxygen. For samples PtC20, PtC30, and PtC10 in 100% oxygen the radius doubles after exposure to the ADT, and correspond to a quadrupling of the $dE/d\log i$-slope with respect to the approximately 65 mV slope at 10 mA cm^{-2}. A quadrupling is what is predicted for a transition from kinetic-migration control to a process governed also by oxygen diffusion in agglomerates, Table 2. This and the half-order dependence on oxygen deduced from Figure 5 thus indicates that oxygen transport also becomes influential on the current-voltage characteristics. However, the semicircle-radius for the PtC10 in 13% oxygen experiences an even larger increase, and the semicircle radius in a Tafel impedance-plane plot would be approximately 0.3 V for this data set (1.5 Ω cm^2×0.2 A cm^{-2}). This therefore indicates a $dE/d\log i$-slope of six times that at 10 mA cm^{-2} (Figure 4).

The reason for the increase in the $dE/d\log i$-slope being significantly larger at low partial pressure of oxygen than at high may be discussed qualitatively in terms of the expression for the current in a single agglomerate, I_a given by the equation [42, Eq. (5)]

$$I_a = -4\pi n F \mathcal{D}_O R_a c_O^s \left[\phi R_a \coth(\phi R_a) - 1 \right] \qquad (6)$$

where n is the number of electrons transferred in the electrochemical reaction, $\mathcal{D}_O$ is the effective diffusivity of oxygen in the agglomerate, R_a the agglomerate radius, c_O^s the (agglomerate) surface concentration of oxygen, and ϕ is given by

$$\phi R_a = \sqrt{\frac{a_a k}{\mathcal{D}_O}} R_a \exp(-2.3\eta/2b_T) \qquad (7)$$

and in which b_T is the Tafel slope (base 10) at the corresponding macroscopic electrode as above, a_a the area of catalyst per unit volume of agglomerate, k the rate constant, and η the local overpotential. (In isolation these equations do of course represent major simplifications with respect to the models on which Table 2 is based.) Eq. (6) and (7) predict a change in the $dE/d\log i$-slope from b_T at $\phi R_a \ll 1$ to $2b_T$ at $\phi R_a \gg 1$. The agglomerate current at the transition between these two regimes, i.e. I_a at $\phi R_a \sim 1$, is thus independent of a_a for any given oxygen concentration. In terms of the local agglomerate current the increased influence of oxygen transport may be due to an increase in the local current density (at constant geometric current density as in Figure 6), in turn either due to fewer agglomerates or a more uneven current distribution in the layer due to a lower conductivity (see below). This would bring the local agglomerate

current closer to that at $\phi R_a \sim 1$ and therefore increase the sensitivity towards c_O.

3.4. Morphological changes due to ADT

Figure 7 shows the SEM images of cathode cross-sections for pristine and degraded catalytic layers before and after the ADT. As expected, there are clear differences in the average thickness between the three fresh CCLs due to the differences in carbon content. The layers were thinner after the experiments, which may be due to carbon corrosion or MEA reorganization. The average thicknesses of the electrodes decrease 35%, 37% and 36% for the PtC10, PtC20 and PtC30, respectively and the thickness reduction is thus quite similar for all samples. No dramatic changes in terms of morphology of the cathodes were observed, however.

The CCLs not only experience a considerable decrease in the average pore size, but also in the pore size distribution (also estimated from SEM images), as seen in Figure 8. There are clear indications that the majority of the pores larger than 100 nm disappear during the ADT and there is a larger count of pores smaller than 50 nm.

As Figure 8 shows, the reduction of pore size for the catalysts are not significantly different for the different thicknesses. It is interesting to compare the results in Figure 8 with those in Figure 1. According to the latter result the degree of corrosion suffered by the carbon should be very dependent on the Pt-to-carbon ratio, in agreement with reports on catalytic effects of Pt on carbon corrosion [51, 52], whereas the morphological changes observed due to the ADT do not display any significant differences on this ratio. However, carbon corrosion is most significant in the higher potential region (> 1 V) in which is also the least sensitive to the Pt-to-carbon ratio [53, 54]. Comparing Figures 1 and 8 we conclude that the carbon corrosion takes place in the higher potential range during the ADT.

Figure (8) does not lend credibility to the hypothesis that the different behavior of the ADT-subjected PtC10 (Figures 5 and 6) from the other two samples is due to a change in the transition potential for doubling of the $dE/d\log i$-slope based on Eq. (6). If this was the case, the rather similar carbon corrosion of the three samples displayed in Figure 8 should give a similar behaviour of the ADT-subjected samples in low-O$_2$ containing atmospheres. This leaves us with the kinetic explanation based on Figure 6 as the most likely reason for this difference.

3.5. In-situ CO stripping and half-cell measurements in N_2

Figure 10 shows the results for in-situ CO stripping of the three samples before after the ADT.

For the pristine samples, the CO oxidation peaks are narrow and unimodal for PtC10 and PtC20, but show a minor shoulder for PtC30. After the ADT however, all samples develop a double peak in the CO oxidation region and the main peak is negatively shifted . Such features have been shown by Maillard et al. [55] to accompany agglomeration of catalysts, as has been thoroughly documented also by others [56]. It is therefore more than likely that the peak shift and the shoulder apparent in Figure 9 are related to agglomeration induced by the ADT.

Table 3 summarizes the in-situ CO stripping results for the three MEAs before and after the ADT. Initially PtC20 has the highest ECA, slightly more than that of PtC10, while sample PtC30 has the lowest ECA. For PtC30 this correlates with the larger particle size (Table 1) of this catalyst. The ECA of PtC10 is lower than that of PtC20, however, although the particle size of the former is smaller than that of the latter. While the difference is rather small, we assume that this is related to factors not captured by size alone such as shape, agglomeration, experimental uncertainty etc. As seen in Table 3, the loss of ECA is 46%, 47% and 50% for PtC10, PtC20 and PtC30, respectively. It thus appears that the almost 50% decrease in ECA translates to a disproportionately lesser loss in the performance, but is approximately independent of the CCL thickness.

Combining the areas from Table 3 with the catalyst loading we obtain current densities in the low-current regime less than or around $1 \, \text{mA cm}^{-2}$ per real catalyst area. This is below or at the critical current for the change in Tafel slope in the data of Parthasarathy *et al.* [49]. However, this assumes that the total current is distributed evenly over the entire catalyst area. After the ADT the catalysts appear to be much more affected by oxygen diffusion in the agglomerates than prior to the ADT. The current distribution within the agglomerates will therefore be more and more uneven the lower the catalyst area per volume, a_a. PtC10 is the catalyst which already at the outset has the lowest catalyst area per volume. The six times larger $dE/d\log i$-slope in sample PtC10 in 13% oxygen may therefore be due to a local current density exceeding the critical current density for higher $dE/d\log i$-slope for the ORR [49] on top of the effects of migration and diffusion. da Silva and Ticianelli [12] also invoked higher Tafel slopes (associated with the degree of coverage of oxygen at the platinum surface [57]) in their interpretation of data for carbon-supported Pt catalysts in carbon-cloth electrodes.

EIS in N_2 was performed at 0.35 V vs RHE. In addition to presenting these in impedance-plane plots we also calculated the electrode capacitance, $C_{\text{electrode}}$, defined as $1/[Im(Z) \times \omega]$ [58]. Figure 10 (a), Figure 10 (c) and Figure 10 (e) show the electrode capacitance plotted as a function of frequency for PtC10, PtC20 and PtC30, respectively. Figure 10 (b), Figure 10 (d) and Figure 10 (f) present the impedance-plane plots, for PtC10, PtC20 and PtC30, respectively.

The EIS data recorded in an N_2 atmosphere were analyzed using Eq. (21) in Ref. [44], according to which the impedance Z is given by

$$Z = \frac{1}{\tanh(\alpha L_{\text{ct}})} \frac{1}{\alpha \kappa_{\text{e}}} \text{ with } \alpha^2 = \frac{A_{\text{dl}} C_{\text{dl}} (1 - \epsilon_1)(1 - \epsilon_2)}{\kappa_{\text{e}}} i\omega \tag{8}$$

where κ_{eff} is the effective proton conductivity in the catalytic layer, A_{dl} is the catalyst plus carbon specific area per unit volume of carbon, C_{dl} is the double-layer capacitance per unit area of carbon plus catalyst, ϵ_1 is the volume fraction of polymer electrolyte in the agglomerate nucleus, and ϵ_2 is the volume fraction of pores in the catalytic layer. Eq. (8) suggests a 45° line with the real axis of the impedance plane plot at high frequencies, and then a vertical line at low frequencies. Eq. (8) appears to represent the data reasonably well.

In the low-frequecy limit the real part of the impedance $Re(Z)$ becomes [44, 59]

$$\lim_{\omega \to 0} Re(Z) = \frac{L_{\text{ct}}}{3\kappa_{\text{e}}} = \frac{R_i}{3} \tag{9}$$

where κ_{e} is the effective conductivity, R_i is the (area-specific) ionomer resistance of the CCL and L_{ct} is again the cathode thickness. From the imaginary part of the low-frequency limit of Eq. (8) we obtain the following value for electrode capacitance

$$C_{\text{electrode}} = A_{\text{dl}} C_{\text{dl}} (1 - \epsilon_1)(1 - \epsilon_2) L \tag{10}$$

The capacitance and resistance of the electrode were obtained through fitting Eq. (8) to the data and use of Eqs. (9) and (10).

The experimental results display a modest increase in the electrode resistance in all cases as can be seen from the shifts of the low-frequency limit of the impedance due to the ADT. The thinning of the CCL does therefore not translate into smaller resistances across the layers. Instead a decrease in layer conductivity is observed; from Eq. (9) values for κ_{e} in the order of $1 \, \text{S cm}^{-1}$ were

Table 3: ECAs from in-situ CO-stripping before and after ADT. The values were obtained through numerical integration of the CO-stripping peak with the integrated current from the baseline voltammogram in the same potential region subtracted. The corresponding charges were converted to ECA through Eq. (2).

Sample	ECA before m^2g^{-1} (CO)	ECA after m^2g^{-1} (CO)	Difference m^2g^{-1}	% decrease
PtC10	40	22	19	46
PtC20	46	25	22	47
PtC30	30	15	15	50

obtained for all samples, and these were consequently reduced by around 50% by the ADT, again for all samples, see Table 4. The resistance decrease is approximately the same for all samples, and therefore the differences between PtC10 and the other two samples in Figure 6 appear not to be caused by differences in how the proton conductivity changes in response to the ADT.

The changes in the capacitance are significant, however, and the capacitances became much larger after the tests than before for all three samples. This is at odds with the decrease in the surface area observed here. Following reference [60], however, the increase in the double layer capacitance may be due to chemical changes due to for example carbon corrosion in the layer, leading to the presence of carbon species with oxygen functionalities assembling at the carbon surface, which in turn lead to larger values for C_{dl} [60]. In fact, the voltammograms in Figure 10 display quite clear signs of an oxidation-reduction process at 0.6 V, indicative of the quinone-hydroquinone redox couple [25, 52, 61]. Apparently, the duration of our experiments is too short to observe the area losses out-competing the changes in the specific values for the double-layer capacity, as was for instance seen in reference [60]. Also, the changes in pore-size distribution in Figure (8) and the reduced κ_e points to an increase in the factor $(1 - \epsilon_1)(1 - \epsilon_2)$.

4. Conclusion

Three Pt/C cathode electrodes for PEMFCs with Pt loadings of 10%, 20%, and 30%, were synthesized by the polyol technique. Electrodes were prepared from these, all containing approximately the same total amount of Pt. That is, the electrodes contained different total amount of carbon and therefore the electrode thicknesses were also different. These electrodes were comprehensively characterized ex-situ (physically and electrochemically) and in a fuel cell set-up before and after being subjected to an accelerated degradation protocol.

We found that the initial electrochemical performance was independent of total carbon content, or equivalently independent of catalyst layer thickness for the range of electrode thicknesses in this study. The results for the fresh samples were compatible with kinetic control at low currents and proton migration in the catalytic layer at high.

The performance of all CCLs experienced a significant decrease when subjected to the accelerated degradation protocol, both in pure oxygen and in diluted oxygen. Polarization curves and impedance spectra recorded in pure oxygen showed a reduction in performance approximately independent of the Pt-to-carbon ratio. In diluted oxygen, however, polarization curves and impedance spectra showed a reduction in performance due to the acceleration test strongly dependent on the Pt-to-carbon ratio. In this case there was a much larger reduction in cell voltage with the catalytic layer containing 10 wt% Pt and 90 wt% carbon than the other two, and the impedance diagrams also showed a much larger increase in the radii of the low-frequency arc for this sample than for the other two.

These results are best interpreted as a transition to a regime controlled both by kinetics, migration, and oxygen diffusion in agglomerates in the sample with the lowest catalyst surface area per volume, much less noticeable in the samples with larger catalyst surface per volume. For the sample with the lowest catalyst area per volume an additional increase in the $dE/d\log i$-slope may be interpreted as due to a change in the Tafel slope for the ORR due to the more uneven current distribution in this sample. These results show that even for a constant loading catalyst layer degradation will manifest itself in different ways depending on the thickness of the catalytic layer.

Carbon corrosion in the catalytic layers appears to be independent of thickness.

Table 4: Capacitance and conductivity from EIS measurements in N_2.

	PtC10		PtC20		PtC30	
	Before	After	Before	After	Before	After
$C_{electrode}$ (mF cm^{-2})	10.8	29.6	7.8	17.1	4.3	6.8
$R_i/3$ (mΩ cm^2)	46.6	56.2	27.9	32.3	14.1	16.4
R_i (mΩ cm^2)	140	169	84	97	42	49
κ_e (S cm^{-1})	1.32	0.71	1.23	0.66	1.18	0.65

[1] V. Mehta, J. S. Cooper, Review and analysis of PEM fuel cell design and manufacturing, J. Power Sources 114 (1) (2003) 32–53. doi:10.1016/S0378-7753(02)00542-6.
URL http://linkinghub.elsevier.com/retrieve/pii/S0378775302005426

[2] I. Bar-On, R. Kirchain, R. Roth, Technical cost analysis for PEM fuel cells, J. Power Sources 109 (2002) 71–75.

[3] S. Kamarudin, W. Daud, A. Md.Som, M. Takriff, A. Mohammad, Technical design and economic evaluation of a PEM fuel cell system, J. Power Sources 157 (2) (2006) 641–649. doi:10.1016/j.jpowsour.2005.10.053.
URL http://linkinghub.elsevier.com/retrieve/pii/S0378775305014473

[4] N. V. Aieta, P. K. Das, A. Perdue, G. Bender, A. M. Herring, A. Z. Weber, M. J. Ulsh, Applying infrared thermography as a quality-control tool for the rapid detection of polymer-electrolyte-membrane-fuel-cell catalyst-layer-thickness variations, J. Power Sources 211 (2012) 4–11. doi:10.1016/j.jpowsour.2012.02.030.
URL http://linkinghub.elsevier.com/retrieve/pii/S0378775312003904

[5] A. J. Steinbach, M. K. Debe, J. Wong, M. J. Kurkowski, A. T. Haug, D. M. Peppin, S. K. Deppe, S. M. Hendricks, E. M. Fischer, A New Paradigm for PEMFC Ultra-Thin Electrode Water Management at Low Temperatures, ECS Transactions 33 (1) (2010) 1179–1188. doi:10.1149/1.3484611.
URL http://ecst.ecsdl.org/cgi/doi/10.1149/1.3484611

[6] A. J. Steinbach, M. K. Debe, M. J. Pejsa, D. M. Peppin, A. T. Haug, M. J. Kurkowski, S. M. Maier-Hendricks, Influence of Anode GDL on PEMFC Ultra-Thin Electrode Water Management at Low Temperatures, ECS Transactions 41 (1) (2011) 449–457. doi:10.1149/1.3635579.
URL http://ecst.ecsdl.org/cgi/doi/10.1149/1.3635579

[7] M. Pestrak, Y. Li, S. W. Case, D. A. Dillard, M. W. Ellis, Y.-H. Lai, C. S. Gittleman, The Effect of Mechanical Fatigue on the Lifetimes of Membrane Electrode Assemblies, Journal of Fuel Cell Science and Technology 7 (4) (2010) 041009. doi:10.1115/1.4000629.
URL http://link.aip.org/link/JFCSAU/v7/i4/p041009/s1\&Agg=doi

[8] S. Kundu, M. W. Fowler, L. C. Simon, S. Grot, Morphological features (defects) in fuel cell membrane electrode assemblies, J. Power Sources 157 (2) (2006) 650–656. doi:10.1016/j.jpowsour.2005.12.027.
URL http://linkinghub.elsevier.com/retrieve/pii/S0378775305016964

[9] A. Z. Weber, J. Newman, Effects of Membrane- and Catalyst-Layer-Thickness Nonuniformities in Polymer-Electrolyte Fuel Cells, J. Electrochem. Soc. 154 (4) (2007) B405. doi:10.1149/1.2437062.
URL http://jes.ecsdl.org/cgi/doi/10.1149/1.2437062

[10] E. A. Ticianelli, J. G. Berry, S. Srinivasan, Dependence of performance of solid polymer electrolyte fuel cells with low platinum loading on morphologic characteristics of the elctrodes, J. Appl. Electrochem. 21 (1991) 597 – 605.

[11] M. S. Wilson, High Performance Catalyzed Membranes of Ultra-low Pt Loadings for Polymer Electrolyte Fuel Cells, J. Electrochem. Soc. 139 (2) (1992) L28 – L30. doi:10.1149/1.2069277.
URL http://jes.ecsdl.org/cgi/doi/10.1149/1.2069277

[12] S. L. A. da Silva, E. A. Ticianelli, Studies of limiting polarization behavior of gas diffusion electrodes with different platinum distributions and hydrophobic properties, J. Electroanal. Chem. 391 (1995) 101 – 109.

[13] V. A. Paganini, E. A. Ticianelli, E. R. Gonzalez, Development and electrochemical studies of gas diffusion electrodes for polymer electrolyte fuel cells, J. Appl. Electrochem. 26 (1996) 297 – 304.

[14] T. R. Ralph, G. A. Hards, J. E. Keating, S. A. Campbell, D. P. Wilkinson, M. Davis, J. St-Pierre, M. C. Johnson, Low cost electrodes for proton exchange membrane fuel cells, J. Electrochem. Soc. 144 (1997) 3845 – 3857.

[15] M. A. Saha, D. Malevich, E. Halliop, J. G. Pharoah, B. A. Peppley, K. Karan, Low cost electrodes for proton exchange membrane fuel cells, J. Electrochem. Soc. 158 (2011) B562 – 567.

[16] E. Gloaguan, F. Andolfatto, R. Durand, P. Ozil, Kinetic study of electrochemical reactions at catalyst-recast ionomer interfaces from thin active layer modelling, J. Appl. Electrochem. 24 (1994) 863 – 869.

[17] M. Eikerling, A. Kornyshev, Modelling the performance of the cathode catalyst layer of polymer electrolyte fuel cells, J. Electroanal. Chem. 453 (1-2) (1998) 89–106. doi:10.1016/S0022-0728(98)00214-9.
URL http://linkinghub.elsevier.com/retrieve/pii/S0022072898002149

[18] H. Dohle, K. Wippermann, Experimental evaluation and semi-empirical modeling of U/I characteristics and methanol permeation of a direct methanol fuel cell, J. Power Sources 135 (1-2) (2004) 152–164. doi:10.1016/j.jpowsour.2004.04.014.
URL http://linkinghub.elsevier.com/retrieve/pii/S0378775304005117

[19] D. Song, Q. Wang, Z. Liu, T. Navessin, M. Eikerling, S. Holdcroft, Numerical optimization study of the catalyst layer of PEM fuel cell cathode, J. Power Sources 126 (1-2) (2004) 104–111. doi:10.1016/j.jpowsour.2003.08.043.
URL http://linkinghub.elsevier.com/retrieve/pii/S0378775303010000

[20] D. Song, Q. Wang, Z. Liu, M. Eikerling, Z. Xie, T. Navessin, S. Holdcroft, A method for optimizing distributions of

Nafion and Pt in cathode catalyst layers of PEM fuel cells, Electrochimica Acta 50 (16-17) (2005) 3347–3358. doi:10.1016/j.electacta.2004.12.008.
URL http://linkinghub.elsevier.com/retrieve/pii/S0013468604012216

[21] A. Abedini, B. Dabir, M. Kalbasi, Experimental verification for simulation study of Pt/CNT nanostructured cathode catalyst layer for PEM fuel cells, Int. J. Hydrogen Energy 37 (10) (2012) 8439–8450. doi:10.1016/j.ijhydene.2012.02.093.
URL http://linkinghub.elsevier.com/retrieve/pii/S0360319912004570

[22] N. Khajeh-Hosseini-Dalasm, M. Kermani, D. G. Moghaddam, J. Stockie, A parametric study of cathode catalyst layer structural parameters on the performance of a PEM fuel cell, Int. J. Hydrogen Energy 35 (6) (2010) 2417–2427. doi:10.1016/j.ijhydene.2009.12.111.
URL http://linkinghub.elsevier.com/retrieve/pii/S0360319909020394

[23] S. Obut, E. Alper, Numerical assessment of dependence of polymer electrolyte membrane fuel cell performance on cathode catalyst layer parameters, J. Power Sources 196 (4) (2011) 1920–1931. doi:10.1016/j.jpowsour.2010.10.030.
URL http://linkinghub.elsevier.com/retrieve/pii/S037877531001757X

[24] M. Wilson, S. Gottesfeld, Thin-film catalyst layers for polymer electrolyte fuel cell electrodes, Journal of Applied Electrochemistry 22 (1992) 1–7.

[25] K. Kinoshita, Carbon: Electrochemical and Physicochemical Properties, Wiley-Blackwell, 1998.

[26] M. F. Mathias, R. Makharia, H. A. Gasteiger, J. J. Conley, T. J. Fuller, C. J. Gittleman, S. S. Kocha, D. P. Miller, C. K. Mittelsteadt, T. Xie, S. G. Yan, P. T. Yu, Two Fuel Cell Cars In Every Garage?, The Electrochemical Society Interface 14 (3) (2005) 24–35.

[27] R. A. Silva, T. Hashimoto, G. Thompson, C. Rangel, Characterization of MEA degradation for an open air cathode PEM fuel cell, Int. J. Hydrogen Energy 37 (8) (2012) 7299–7308. doi:10.1016/j.ijhydene.2011.12.110.
URL http://linkinghub.elsevier.com/retrieve/pii/S0360319911028333

[28] J. Newman, C. W. Tobias, Theoretical Analysis of Current Distribution in Porous Electrodes, J. Electrochem. Soc. 109 (12) (1962) 1183. doi:10.1149/1.2425269.
URL http://jes.ecsdl.org/cgi/doi/10.1149/1.2425269

[29] J. Jiang, B. Yi, Thickness effects of a carbon-supported platinum catalyst layer on the electrochemical reduction of oxygen in sulfuric acid solution, J. Electroanal. Chem. 577 (2005) 107–115. doi:10.1016/j.jelechem.2004.11.022.

[30] G. Cao, Y. Wang, Nanostructures and Nanomaterials: Synthesis, Properties and Applications, Imperial College Press, London, 2004.

[31] Z. Yang, S. Ball, D. Condit, M. Gummalla, Systematic Study on the Impact of Pt Particle Size and Operating Conditions on PEMFC Cathode Catalyst Durability, J. Electrochem. Soc. 158 (11) (2011) B1439. doi:10.1149/2.081111jes.
URL http://jes.ecsdl.org/cgi/doi/10.1149/2.081111jes

[32] Doe cell component accelerated stress test protocols for pem fuel cells, Tech. rep., U.S. Department of Energy, https://energy.gov/eere/fuelcells/downloads/fuel-cell-tech-team-accelerated-stress-test-and-polarization (2007).

[33] C. A. Reiser, L. Bregoli, T. W. Patterson, J. S. Yi, J. D. L. Yang, M. L. Perry, T. D. Jarvi, A reverse-current decay mechanism for

[34] Y. Wang, J. Ren, K. Deng, L. Gui, Y. Tang, Preparation of Tractable Platinum , Rhodium , and Ruthenium Nanoclusters with Small Particle Size in Organic Media, Chemistry of Materials (9) (2000) 1622–1627.

[35] M. Darab, M. Thomassen, S. Sunde, The Effect of Synthesis Methods on the Electrochemical Activity and Durability of Carbon Supported Platinum Nanoparticles as Electrocatalysts for PEMFC, ECS Transactions 41 (1) (2011) 1067–1078. doi:10.1149/1.3635639.
URL http://ecst.ecsdl.org/cgi/doi/10.1149/1.3635639

[36] T. Vidaković, M. Christov, K. Sundmacher, The use of CO stripping for in situ fuel cell catalyst characterization, Electrochimica Acta 52 (18) (2007) 5606–5613. doi:10.1016/j.electacta.2006.12.057.

[37] A. Lundblad, Materials Characterization of Thin Film Electrodes for PEFC Survey of Methods and an Example, J. New Mater. Electrochem. Sys. 28 (7) (2004) 21–28.

[38] W. Rasband, Imagej, u.s. national institutes of health.
URL http://imagej.nih.gov/ij/

[39] H. A. Gasteiger, S. S. Kocha, B. Sompalli, F. T. Wagner, Activity benchmarks and requirements for pt, pt-alloy, and non-pt oxygen reduction catalysts for pemfcs, App. Catal. B: Environmental 56 (2005) 9 – 35.

[40] B. M. Rush, J. A. Reimer, E. J. Cairns, Nuclear Magnetic Resonance and Voltammetry Studies of Carbon Monoxide Adsorption and Oxidation on a Carbon-Supported Platinum Fuel Cell Electrocatalyst, J. Electrochem. Soc. 148 (2) (2001) A137. doi:10.1149/1.1342164.

[41] P. Ferreira-Aparicio, M. Folgado, L. Daza, High surface area graphite as alternative support for proton exchange membrane fuel cell catalysts, J. Power Sources 192 (1) (2009) 57–62. doi:10.1016/j.jpowsour.2008.12.003.
URL http://linkinghub.elsevier.com/retrieve/pii/S0378775308023136

[42] M. L. Perry, J. Newman, E. J. Cairns, Mass Transport in Gas-Diffusion Electrodes: A Diagnostic Tool for Fuel-Cell Cathodes, J. Electrochem. Soc. 145 (1) (1998) 5. doi:10.1149/1.1838202.
URL http://jes.ecsdl.org/cgi/doi/10.1149/1.1838202

[43] F. Jaouen, G. Lindbergh, G. Sundholm, Investigation of mass-transport limitations in the solid polymer fuel cell cathode, J. Electrochem. Soc. 149 (4) (2002) A437.

[44] F. Jaouen, G. Lindbergh, K. Wiezell, Transient Techniques for Investigating Mass-Transport Limitations in Gas Diffusion Electrodes : I. Modeling the PEFC Cathode, J. Electrochem. Soc. 150 (12) (2003) A1711. doi:10.1149/1.1624294.
URL http://jes.ecsdl.org/cgi/doi/10.1149/1.1624295

[45] M. Darab, P. K. Dahlstrøm, M. S. Thomassen, F. Seland, S. Sunde, Dynamic electrochemical impedance spectroscopy of Pt/C-based membrane-electrode assemblies subjected to cycling protocols, J. Power Sources 242 (2013) 447–454. doi:10.1016/j.jpowsour.2013.05.105.
URL http://linkinghub.elsevier.com/retrieve/pii/S0378775313008951

[46] K. Wiezell, N. Holmström, G. Lindbergh, Studying low-humidity effects in pefcs using eis ii. modeling, J. Electrochem. Soc. 154 (8) (2007) F379 – F392.

[47] N. Holmström, K. Wiezell, G. Lindbergh, Studying lowhumidity effects in pefcs using eis i. experimental, J. Electrochem. Soc. 159 (2012) F369 – F378.

[48] K. Wiezell, P. Gode, G. Lindbergh, Steady-state and eis investi-

gations of hydrogen electrodes and membranes in polymer electrolyte fuel cells. i. modeling, J. Electrochem. Soc. 153 (2006) A749 – A758.

[49] A. Parthasarathy, S. Srinivasan, J. A. Appleby, C. R. Martin, Pressure Dependence of the Oxygen Reduction Reaction at the Platinum Microelectrode/Nafion Interface: Electrode Kinetics and Mass Transport, J. Electrochem. Soc. 139 (10) (1992) 2856. doi:10.1149/1.2068992.
URL http://jes.ecsdl.org/cgi/doi/10.1149/1.2068992

[50] H. Wroblowa, M. L. BRao, A. Damjanovic, J. O. Bockris, Adsorption and kinetics at platinum electrodes in the presence of oxygen at zero net current, J. Electroanal. Chem. 15 (1967) 139 – 150.

[51] B. Wickman, H. Grönbeck, P. Hanarp, B. Kasemo, Corrosion induced degradation of pt/c model electrodes measured with electrochemical quartz crystal microbalance, J. Electrochem. Soc. 157 (2010) B592 – B598.

[52] Y.-C. Park, K. Kakinuma, M. Uchida, H. Uchida, Deleterious effects of interim cyclic voltammetry on pt/carbon blackcatalyst degradation during start-up/shutdown cycling evaluation, Electrochimica Acta 123 (2014) 84 – 92.

[53] N. Linse, L. Gubler, G. G. Scherer, A. Wokaun, The effect of platinum on carbon corrosion behaviour in polymer electrolyte, Electrochimica Acta 56 (2011) 7541–7549.

[54] J. Speder, A. Zana, I. Spanos, J. J. K. Kirensgaard, K. Mortensen, M. Arenz, On the influence of the pt to carbon ratio on the degradation of highg surface area carbon supported pem fuel cell electrocatalysts, Electrochem. Commun. 34 (2013) 156–156.

[55] F. Maillard, S. Schreier, M. Hanzlik, E. R. Savinova, S. Weinkauf, U. Stimming, Influence of particle agglomeration on the catalytic activity of carbon-supported Pt nanoparticles in CO monolayer oxidation, Phys. Chem. Chem. Phys. 7 (2) (2005) 385–393. doi:10.1039/b411377b.
URL http://xlink.rsc.org/?DOI=b411377b

[56] A. López-Cudero, J. Solla-Gullón, E. Herrero, A. Aldaz, J. M. Feliu, Co electrooxidation on carbon supported platinum nanoparticles: Effect of aggregation, J. Electroanal. Chem. 644 (2010) 117 – 126.

[57] D. Sepa, M. Vojnovic, L. Vracar, A. Damjanovic, Different views regarding the kinetics and mechanisms of oxygen reduction at pt and pd electrodes, Electrochimica Acta 32 (1) (1987) 129 – 134. doi:http://dx.doi.org/10.1016/0013-4686(87)87021-4.
URL http://www.sciencedirect.com/science/article/pii/0013468687870214

[58] E. B. Easton, P. G. Pickup, An electrochemical impedance spectroscopy study of fuel cell electrodes, Electrochimica Acta 50 (12) (2005) 2469–2474. doi:10.1016/j.electacta.2004.10.074.
URL http://linkinghub.elsevier.com/retrieve/pii/S0013468604010758

[59] R. Makharia, M. F. Mathias, D. R. Baker, Measurement of Catalyst Layer Electrolyte Resistance in PEFCs Using Electrochemical Impedance Spectroscopy, J. Electrochem. Soc. 152 (5) (2005) A970. doi:10.1149/1.1888367.
URL http://jes.ecsdl.org/cgi/doi/10.1149/1.1888367

[60] A. P. Young, J. Stumper, E. Gyenge, Characterizing the Structural Degradation in a PEMFC Cathode Catalyst Layer: Carbon Corrosion, J. Electrochem. Soc. 156 (8) (2009) B913. doi:10.1149/1.3139963.
URL http://jes.ecsdl.org/cgi/doi/10.1149/1.3139963

[61] Y. Yang, Z.-G. Lin, In situ ir spectroscopic characterization of surface oxide species on glassy carbon electrodes, J. Electroanal. Chem. 364 (1994) 23 – 30.
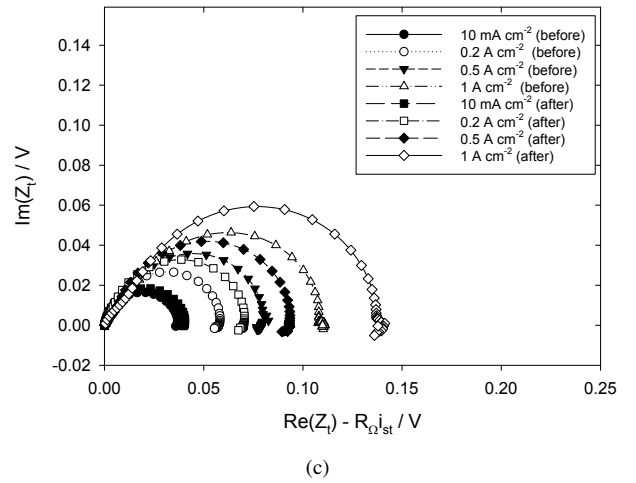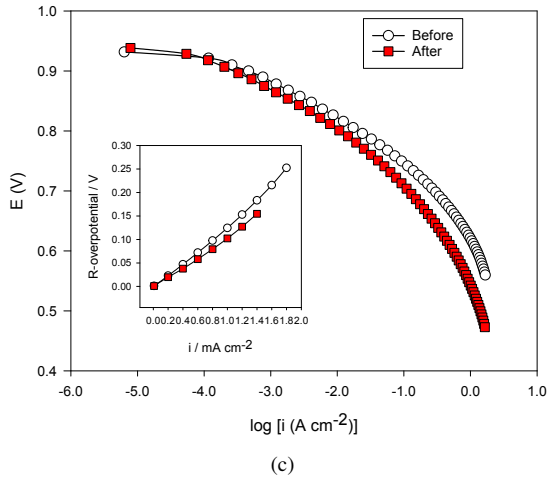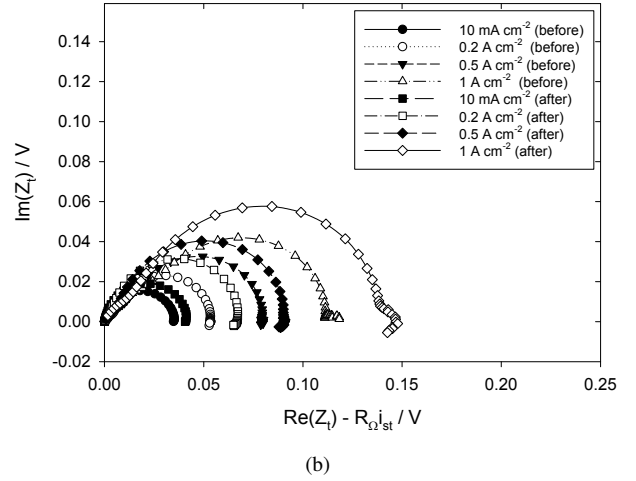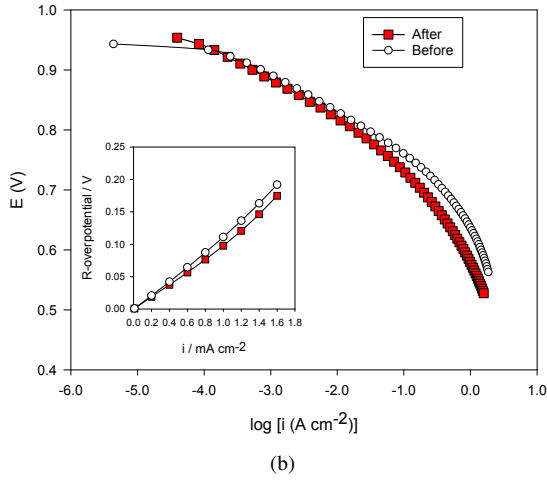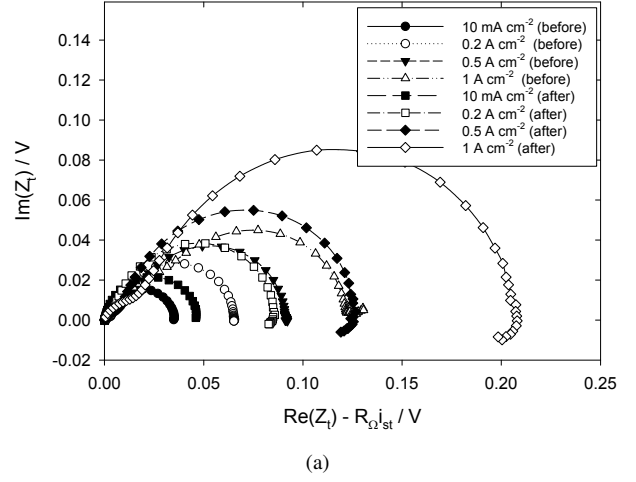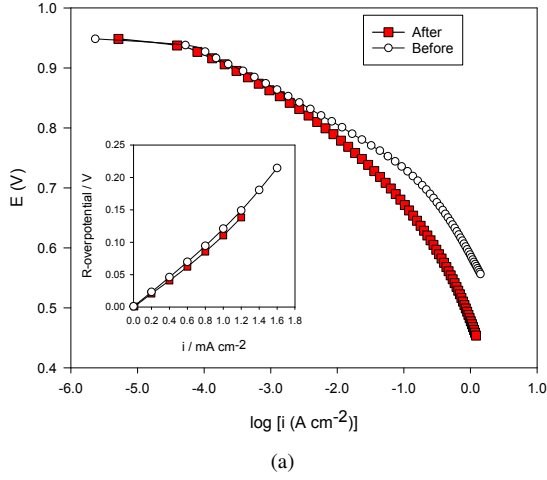
(a)

(b)

(c)

Figure 3: Polarization curves before and after ADT (iR-corrected). (3(a)) PtC10, (3(b)) PtC20 and (3(c)) PtC30. Insets: iR related performance loss for the same samples before and after the ADT. Conditions: temperature 80 °C, fully humidified gases with a flow rate of 60 ml min^{-1} of O_2 fed to the WE and 120 ml min^{-1} of H_2 fed to the CE/RE. The iR-correction is carried out using the Re(Z) in EIS data at 1 kHz.


(a)

(b)

(c)

Figure 4: Impedance-plane plot of Tafel impedance before and after ADT. The high-frequency intercept $R_\infty i_{st}$, where R_∞ is the value of the real part when the imaginary part is equal to zero, has been subtracted from all real values in the plots. a) PtC10 at 1 A cm^{-2}, b) PtC20, same symbols as for PtC10, and c) PtC30. Conditions the same as in Figure 3. EIS conditions: Amplitude 5% of the dc-current, frequency range 10 kHz and 0.1 Hz. Symbols: (●) at 10 mA cm^{-2} before the ADT, (○) at 0.2 A cm^{-2} before the ADT, (▼) at 0.5 A cm^{-2} before the ADT, (△) at 1 A cm^{-2} before the ADT, (■) at 10 mA cm^{-2} after the ADT, (□) at 0.2 A cm^{-2} after the ADT, (◆) at 0.5 A cm^{-2} after the ADT, (◇) at 1 A cm^{-2} after the ADT.
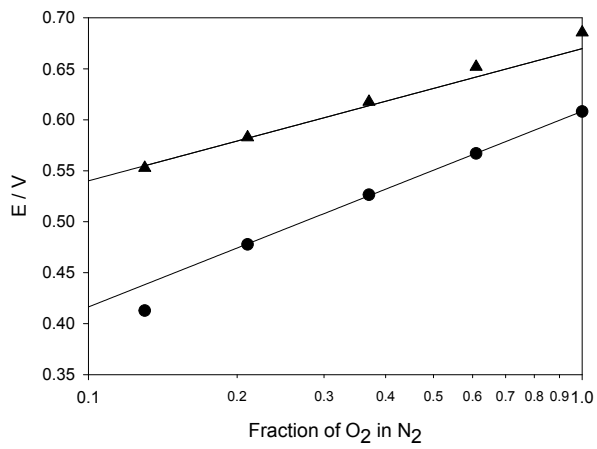
(a)
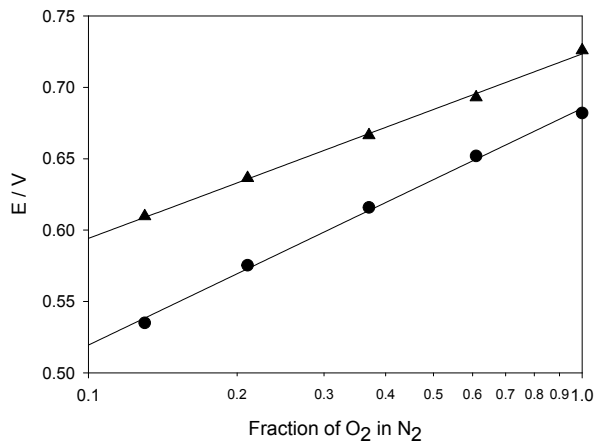
(b)
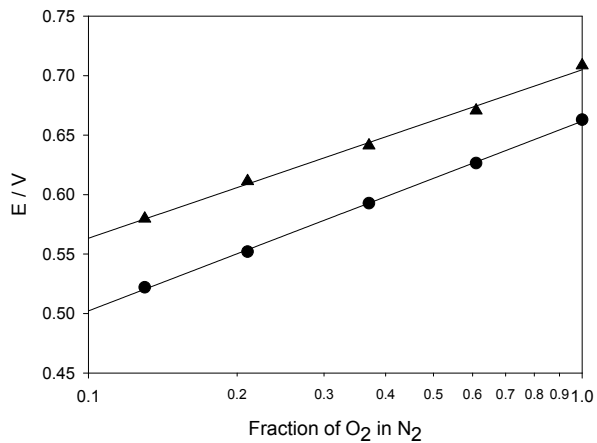
(c)

Figure 5: iR-corrected cell voltage using diluted O_2 at 0.2 A cm^{-2} before and after ADT vs. the logarithm (base 10) of the fraction of oxygen at the cathode. a) PtC10 before (▲) and after (●) the ADT, b) PtC20 before (▲) and after (●) the ADT, and c) PtC30 before (▲) and after (●) the ADT. Conditions: atmospheric pressure, temperature 80 °C, fully humidified gases with a flow rate of 60 ml min^{-1} of diluted O_2 fed to the WE and 120 ml min^{-1} of H_2 fed to the CE/RE.
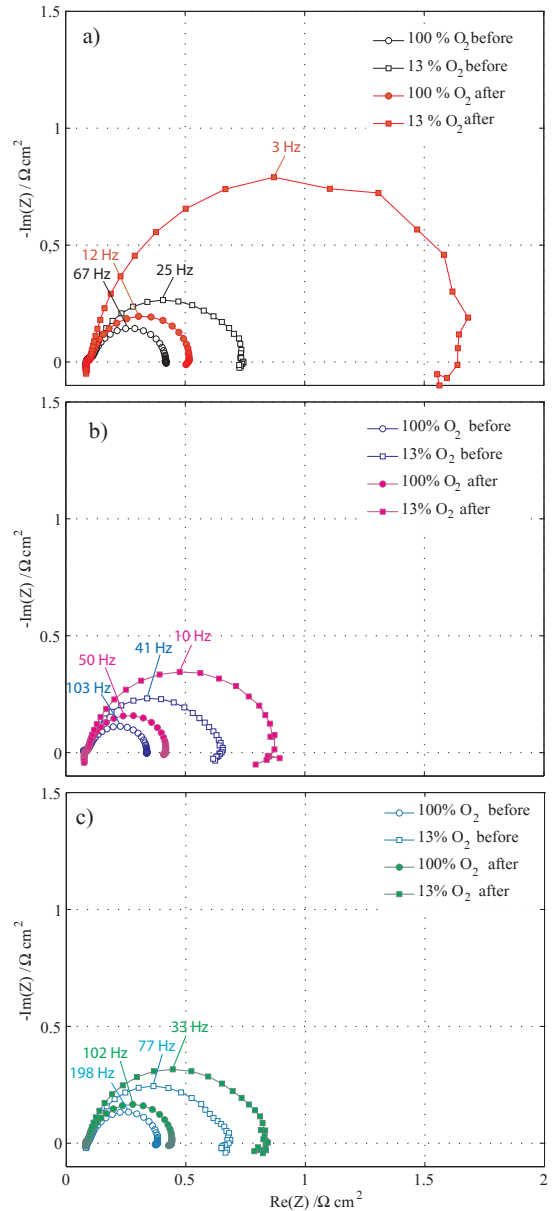
Figure 6: Impedance-plane plots for diluted O_2 at 0.2 A cm^{-2} before and after ADT. a) PtC10, b) PtC20 and c) PtC30. Conditions: atmospheric pressure, 80 °C temperature, fully humidified gases with a flow rate of 60 ml min^{-1} of O_2 fed to the WE and 120 ml min^{-1} of H_2 fed to the CE/RE.
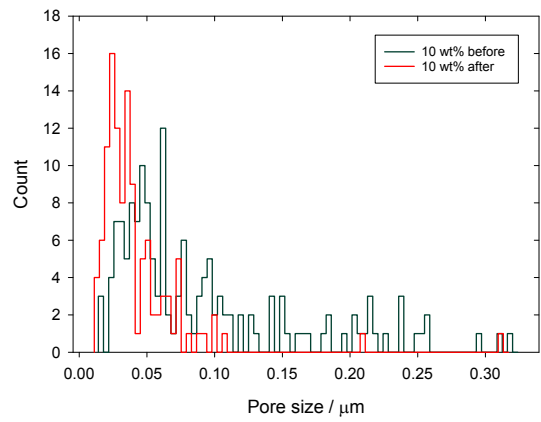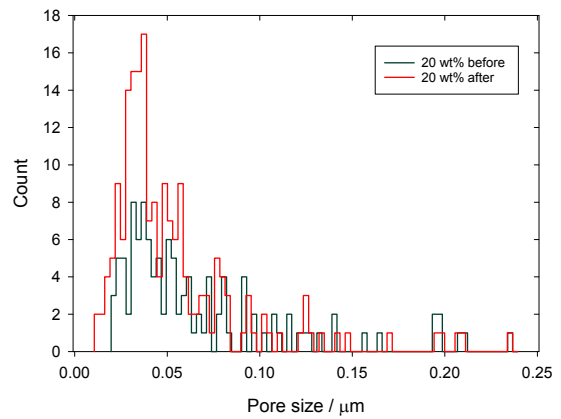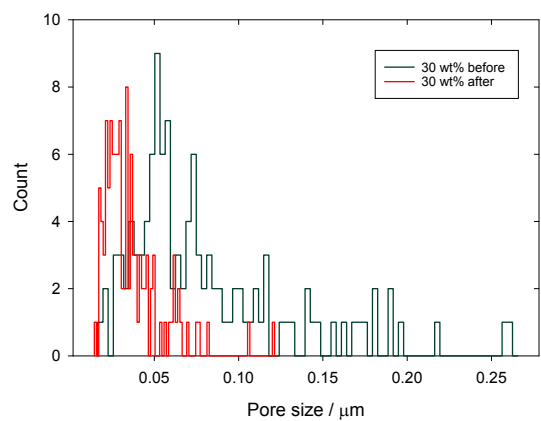
15
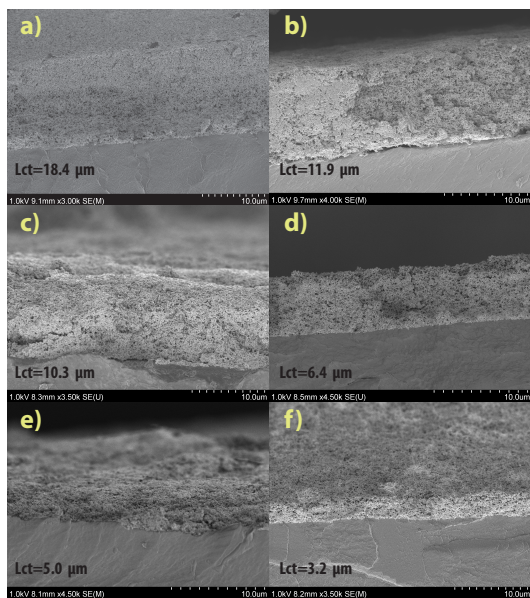
Figure 7: SEM images of cathode cross-sections before and after the ADT: a) PtC10 before, b) PtC10 after, c) PtC20 before, d) PtC20 after, e) PtC30 before and f) PtC30 after. THe estimated catalytic-layer thicknesses are given directly in the images.

(a)

(b)

(c)

Figure 8: Pore size distribution for PtC10 (8(a)), PtC20 (8(b)), and PtC30 (8(c)) estimated from SEM images using image software ImageJ.
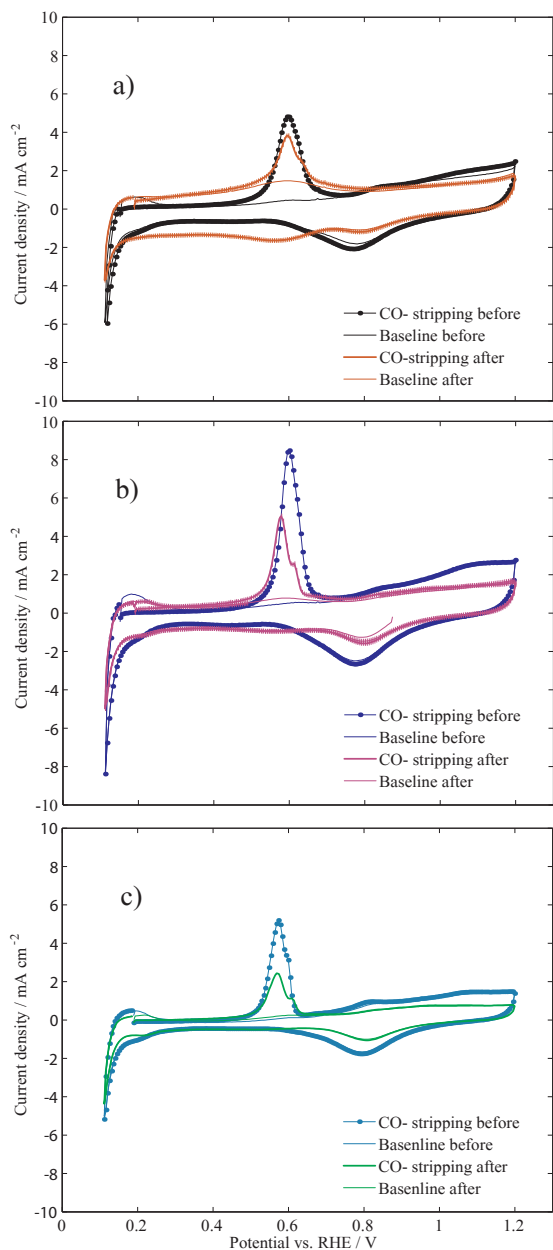
Figure 9: Cyclic voltammetry and CO stripping before and after ADT. a) PtC10, b) PtC20 and c) PtC30. Conditions: temperature 80 °C, fully humidified gases with a flow rate of 60 ml min^{-1} of N$_2$ fed to the WE and 120 ml min^{-1} of 5 % H$_2$/Ar fed to the CE/RE, sweep rates 20 mV s^{-1}.
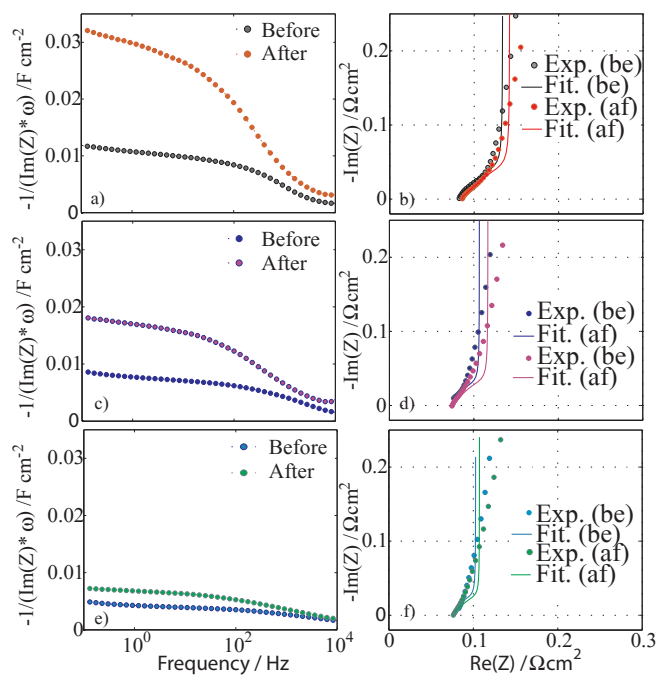

Figure 10: EIS measurements in N$_2$ before and after ADT: a) PtC10 capacitance plot, b) PtC10 impedance-plane plot, c) PtC20 capacitance plot, d) PtC20 impedance-plane plot, e) PtC30 capacitance plot and f) PtC30 impedance-plane plot. Conditions: the same as in Figure 10. EIS conditions: alternating voltage 10 mV (top) at 0.376 V vs. RHE by varying the frequency between 10 kHz and 0.1 Hz.